Numerical simulation of small pool fires incorporating liquid fuel motion

Kazui Fukumoto[a,b,*], Jennifer X. Wen[b], Manhou Li[a], Yanming Ding[d], and Changjian Wang[a,c,*]

[a]School of Civil Engineering, Hefei University of Technology, China

[b]Warwick FIRE, School of Engineering, University of Warwick, United Kingdom

[c]Anhui International Joint Research Center on Hydrogen Safety, Hefei, 230009, China

[d]Faculty of Engineering, China University of Geosciences, Wuhan, 430074, China

Abstract

For small-scale pool fires, the pair of vortices was experimentally observed in the liquid pool. The first vortex appeared just close to a container wall, and the second one was observed slightly away from the first vortex. To investigate the underlying physics associated with the above phenomenon, large eddy simulations (LES) of small methanol pool fires coupled with liquid fuel convective flow were conducted. A three-dimensional (3-D) liquid phase model is newly developed incorporating the effects of thermocapillary Marangoni convection, buoyancy, shear stress and evaporation in the liquid phase. For the gas phase, combustion is modelled by the extended eddy dissipation concept model with the laminar combustion model based on a viscous diffusion rate to consider laminar-turbulence transition. The predictions were in reasonably good agreement with the experimentally measured local mass burning rate, flame height and distributions of liquid temperature. The pair of vortices were captured when sufficiently fine grid resolutions were used. The predicted changing trend in the mass burning rate with the container bottom temperature is also in line with the measurements. The effects of side walls, thermocapillary force and shear stress on the burning rate is analysed. The numerical tests conducted with the validated model also highlights some interesting effect of neglecting gravity in the with the liquid fuel.

Keywords

Pool fire, gas-liquid approach, burning rate, thermocapillary force, large eddy simulation

Corresponding authors: chjwang@hfut.edu.cn, fukumoto@hfut.edu.cn

Nomenclature

a_{rad}	absorption coefficient [m^{-1}]
Cp	heat capacity at constant pressure [J/(kg·K)]
d	pool depth [m]
D	effective diffusion coefficient [m^2/s]
g	gravitational acceleration [m/s^2]
h	heat/sensible enthalpy [J/kg]
h_{mass}	mass transfer coefficient [m/s]
h_{conv}	convective heat transfer coefficient [$W/(K \cdot m^2)$]
h_{vap}	heat of vaporisation [J/kg]
x_f	flame height (length) [m]
L	representative length or length (if no subscript) [m]
Le	Lewis number
$\dot{m}$	mass flow rate/mass burning rate [kg/s]
m''	mass burning rate [$kg/(s \cdot m^2)$]
m'''	mass burning rate per volume [$kg/(s \cdot m^3)$]
M	molecular weight
p	pressure [N/m^2]
p_{dyn}	dynamic pressure [N/m^2]
q	heat release rate [W]
q'''	heat release rate per volume [W/m^3]
q''_{rad}	radiative heat flux [W/m^2]
q''_{conv}	convective heat flux [W/m^2]
r	radius of pool [m]

r_{rad} reflectivity

R gas constant [J/kmol/K]

Re Reynolds number

R_o Criterion for flame volume

S Surface area [m^2]

Sc Schmidt number

Sh Sherwood number

t time [s]

T temperature [K]

T_b boiling point [K]

T_{bot} fuel temperature at the pool bottom [K]

T_{Inter} interface (surface) temperature [K]

u velocity or velocity scale [m/s]

V Volume

x_f flame height [m]

x_j coordinate in j direction [m]

X volume fraction

Y mass fraction

Z mixture fraction

Greek

α thermal diffusivity [m^2/s]

Δ_{dep} depth from interface [m]

ε_{rad} emissivity

η_{rad} transmissivity

λ thermal conductivity [W/(m·K)]

ρ	density [kg/m^3]
μ	viscosity [kg/(m·s)]
σ_{Boltz}	Stefan Boltzmann constant [W/(m^2·K^4)]
σ_{Mar}	surface tension [N/m]
τ	time scale [s]

subscripts

b	boiling
diff	diffusion
EDC	EDC model
f	flame
fu	fuel
First	first cell from the interface
i, *j*, *k*	coordinate indexes
Inter	interface
liq	liquid
rad	radiation/radiative
conv	convection/convective
solid	solid (pool wall)
SGS	sub grid scale
tan	tangential direction
t	turbulence/turbulent
vap	vaporization/vapor
$\tilde{\phi}$	density weighted average
$\bar{\phi}$	time average

1. Introduction

Liquid pool fires are one of the most fundamental fire scenarios, which attracted considerable attention [1–7]. Weckman and Strong [1] investigated turbulence structures of a medium scale methanol pool fire, providing detailed measurements of the velocity, temperature, turbulent kinetic energy and turbulent Reynolds number. Vali et al. [2] investigated the influences of base temperature of the liquid fuel and vessel materials on the burning rate and flame height of a small methanol pool fire. They found that the burning rate and flame height increased with the increase in the base temperature of the liquid fuel. Vali et al. [3] further studied the influences of the convection within a pool, confirming the existence of two vortices near the side wall of the container. Sun et al. [4] studied the behaviour of a circular ring thin-layer pool fire and found that the burning rate changed with the increase of the inner and outer diameters of the circular ring pool.

Some numerical simulations have also been reported. Wen et al. [5] performed a medium-scale methanol pool simulation using the Fire Dynamic Simulator (FDS) [6] developed by the Naitonal Institute of Standards in the USA. Wang et al. [7] predicted a medium scale pool fire using FireFOAM [8], a large eddy simulation (LES) based fire simulation solver within open source computational fluid dynamics (CFD) code OpenFOAM [9]. The predicted temperature and velocity fields were found to be in reasonably good agreement with McCaffrey's measurements [10]. Maragkos et al. [11] modified FireFOAM 2.2.x to consider the effects of non-unity Lewis numbers and thermal diffusion and implemented the dynamic Smagorinsky model with a variable turbulent Pradtl number approach for pool fires.

Some researchers performed coupled pool fire with one-dimensional (1-D) liquid phase simulation. Prasad et al. [14] investigated structures and energetics of a pool fire with an axisymmetric gas-liquid coupled approach and achieved reasonably good agreement with the measurements for the temperature and burning rate. Novozhilov and Koseki [15] developed a gas-liquid coupled approach

to predict the burning rates for small to medium scale pool fires. Although the predictions were broadly consistent with several experimental measurement; they were found to be strongly dependent on a soot conversion factor. Sikanen and Hostikka [16] investigated the effect of in-depth radiation absorption in liquid fuels and reported on its significant effect.

As described above, Vali et al. [3] reported the appearance of two vortices close to the container side wall. The first vortex could be attributed to two factors: (i) an upward flow owing to buoyancy force induced by the wall heated by a fire and (ii) convection caused by shear stress owing to a gas flow on the pool surface. The mechanisms of the second vortex was still not clear, but it was postulated that shear stress owing to gas recirculation near the pool centre dragged a liquid flow from the centre to the pool wall. The authors [17] later suggested that heat conduction from the container side wall influenced the burning rate for small-scale pool fires.

The above findings suggested that the liquid flow motion within the pool might have some influences on the pool fire burning rate and fire dynamics. Such effects warrant further investigation. The objectives of the present study are to develop and validate a coupled gas-liquid approach to capture the burning rate, flame height, liquid temperature and flow motion in a pool; and use the validated model to gain insight about the effect of side walls, thermocapillary force and shear stress on the pool fire mass burning rate. As 1-D liquid phase simulation cannot capture heat conduction through the container side wall, 2-D or 3-D governing equations will be solved for the liquid phase.

2. Physical problem

Figure 1 summarizes the underlying physics of small pool fires, where turbulent and laminar flames co-exist. The pool surface receives both convective and radiative heat transfer from the flame and in the meantime it also emits radiative heat flux. Near the interface, liquid flow is induced by the gradients in the shear stress. While the liquid fuel evaporates at the interface, a pair of vortices were observed in previous experiments [3]. Their existence enhances heat and mass transfer. Due to the

density gradient induced by the temperature differences, the liquid fuel with the large density moves downward, whereas that with the small density goes upward. In-depth radiation occurs owing to the transparency of the liquid fuel. Heat transfers owing to convection and diffusion occurs from the top to bottom while mass and heat are supplied from the bottom of the container. As the flame gradually heats up the side wall of the container, this might also have some influences on the fuel evaporation. Such complicate processes cannot be captured by the previously reported 1-D evaporation models [14–16] as they do not consider shear stress balance, liquid motion, buoyancy and heat transfer from the side wall of a vessel. However, the extent of the relative influences of these factors is unclear and their quantification is also one of the objectives of the present study.

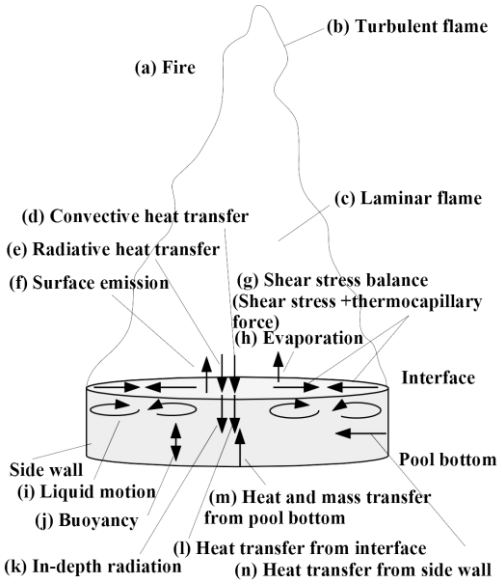

Fig. 1 Physics of small pool fires.

It should be noted that the present study is focused on the steady state condition as in the experiment of Vali et al. [3]. Transient pool fires are more complex, involving (i) initial growth, (ii) steady burning stage, (iii) boiling burning and (iv) decay stages [30]. In most laboratory pool fire tests, there were no continuous fuel supply to maintain the pool height. The lip height and the mass burning rate changed with time. In phases (iii), bubbles formed due to evaporation would enhance

heat exchange with the side walls. Namely, to better capture the transient pool fire scenarios, a change in a lip height and bubble motion should be considered.

3. Methodology

The in-house version of FireFOAM 2.2.x, which contains the authors' previous developments [12,18,19,22] is employed. The momentum and continuity equations are solved by Pressure-Implicit with Splitting of Operators (PISO) with the outer iteration (termed PIMPLE [9]). The energy and species equations are also solved. Since small pool fires involve laminar to turbulent transition near the pool surface, the dynamic Smagorinsky model [20,21] is used for the sub-grid scale turbulence

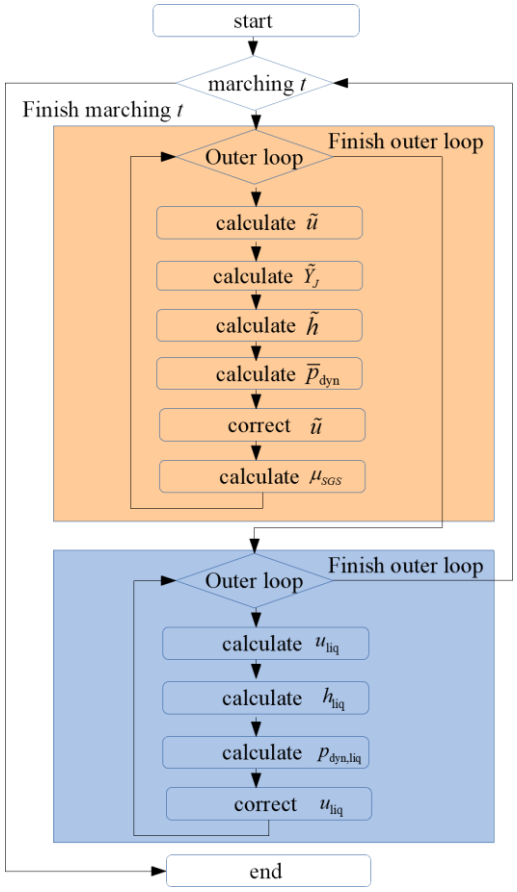

Fig. 2 Flowchart of the solver. Orange and blue parts denote the gas and liquid phases, respectively.

modelling. The methodology for gas phase modelling was the same as presented in our previous studies [22]. Some further modifications to facilitate the present study will be introduced in following sections. Figure 2 is a simple flowchart of the FireFOAM solver used. It consists of two PIMPLE algorithms for the gas and liquid phases denoted as orange and blue in Fig. 2.

3.1. Combustion modelling

In small scale pool fires, the flame undergoes laminar to turbulent transition [23]. This needs to be considered in modelling the combustion process as denoted as (a) in Fig. 1. Following our previous study [19], the time scale of the laminar combustion reaction τ_{diff} was estimated based on viscous diffusion, whereas the time scale of the turbulent combustion reaction τ_{EDC} was computed by Chen et al.'s modified EDC [12]. The minimum of the two was used as the reaction time scale. The infinitely fast chemistry was used as described in our recent paper [22].

3.2. Radiation modelling

The radiative heat transfer equations were solved using the finite volume discrete ordinates method with the gas radiative properties calculated by the weighted sum of grey gas (WSGG) model [24,25]. The total absorption coefficient for the non-sooty methanol fire is calculated by

$$a_{\text{rad}} = -\frac{\ln(1-\varepsilon_{\text{rad}})}{L_{\text{beam}}} \qquad \text{1/m,} \tag{1}$$

where ε_{rad} is the emissivity calculated by the WSGG model. The mean beam length L_{beam} is calculated from the flame shape, which was estimated from preliminary simulation and approximated as of conical shape. Although the calculation of the mean beam length can be avoided using banded formulations of WSGG, this would increase the computational time by 2.9 times [25]. For simplicity, the flame shape is assumed to be a 'cone' for the beam length L_{beam} calculation:

$$L_{\text{beam}} = \frac{3.6V_{\text{f}}}{S_{\text{f}}} = \frac{3.6V_{\text{f}}}{\pi r_{\text{f}}(r_{\text{f}} + L_{\text{arc,f}})} \qquad \text{m,} \tag{2}$$

where V_{f} is the flame volume, S_{f} is the surface area of the flame, r_{f} is the radius of the cone, and $L_{\text{arc,f}}$ is the arc length of the cone. $L_{\text{arc,f}}$ is given as

$$L_{\text{arc,f}} = \left[H_{\text{f}}^2 + r_{\text{f}}^2 \right]^{0.5} \quad \text{m}, \tag{3}$$

where r_{f} is the radius of the cone (equal to the pool radius), and $L_{\text{arc,f}}$ is the arc length of the cone; the height of the cone H_{f} is given as

$$H_{\text{f}} = \frac{3V_{\text{f}}}{r_{\text{f}}^2 \pi} \quad \text{m}, \tag{4}$$

In the above, V_{f} is computed following Yang et al. [26], who used the following criterion to determine the flame border given as

$$R_{\text{o}} = \frac{1}{1 + s\%Y_{\text{fu}} / \%Y_{\text{O}_2}}, \tag{5}$$

The flame border is at $0 \leq R_{\text{o}} \leq 0.7$ for methanol which is determined to fit the predicted flame height.

3.3. Liquid phase modelling

3.3.1. Governing equations and heat balance

The evaporation model is developed based on that of Ali et al. [27] and Sikanen and Hostikka [16] with some modifications; and extended to 3-D. The governing equations for the liquid phase are similar to those for the gas phase equation as follows:

Continuity equation

$$\frac{\partial \rho_{\text{liq}}}{\partial t} + \frac{\partial \rho_{\text{liq}} u_{j,\text{liq}}}{\partial x_j} = 0, \tag{6}$$

Momentum equation

$$\frac{\partial \rho_{\text{liq}} u_{i,\text{liq}}}{\partial t} + \frac{\partial \rho_{\text{liq}} u_{j,\text{liq}} u_{i,\text{liq}}}{\partial x_j} = \frac{\partial}{\partial x_j}\left[\mu_{\text{liq}} \left(\frac{\partial u_{i,\text{liq}}}{\partial x_j} + \frac{\partial u_{j,\text{liq}}}{\partial x_i} - \frac{2}{3} \frac{\partial u_{k,\text{liq}}}{\partial x_k} \delta_{ij} \right) \right], \\ - \frac{\partial p_{\text{dyn,liq}}}{\partial x_i} - g_j x_j \frac{\partial \rho_{\text{liq}}}{\partial x_i} \tag{7}$$

$$p_{\text{dyn,liq}} = p_{\text{liq}} - \rho_{\text{liq}} g_j x_j \tag{8}$$

Sensible enthalpy equation

$$\frac{\partial \rho_{\mathrm{liq}} h_{\mathrm{liq}}}{\partial t}+\frac{\partial \rho_{\mathrm{liq}} u_{j,\mathrm{liq}} h_{\mathrm{liq}}}{\partial x_j}=\frac{Dp_{\mathrm{liq}}}{Dt}+\frac{\partial}{\partial x_j}\left[\rho_{\mathrm{liq}}\alpha_{\mathrm{liq}}\frac{\partial h_{\mathrm{liq}}}{\partial x_j}\right]-m'''h_{\mathrm{vap}}-\frac{\partial q''_{\mathrm{liq,rad}}}{\partial n}, \tag{9}$$

where $m'''h_{\mathrm{vap}}$ is considered in only the first cell from the interface. Some variables exist in both the liquid and gas phases. For such variables, subscript 'liq' indicates the liquid phase. If it is not stated, a variable is one for the gas phase. h_{liq} is defined as

$$h_{\mathrm{liq}}=\int_{293.15}^{T} Cp_{\mathrm{liq}}\,dT \qquad \text{J/kg} \tag{10}$$

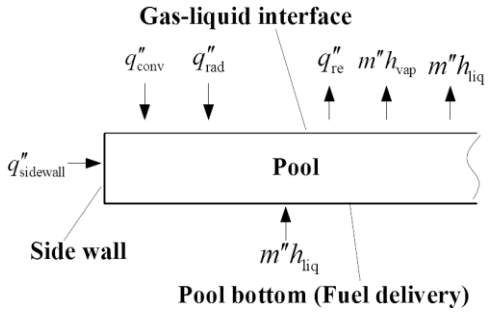

Fig. 3 Overview of heat balance in a small pool fire

Figure 3 gives an overview of the heat balance in a small pool fire, which is considered by boundary and interface conditions. q''_{conv} is the convective heat flux, q''_{rad} is the radiative heat flux, q''_{re} is the re-radiative heat flux owing to surface emission and reflection, q''_{sidewall} is the conductive heat flux from a wall, $m''h_{\mathrm{vap}}$ is the enthalpy loss per time owing to vaporisation, $m''h_{\mathrm{liq}}$ is the enthalpy gain/loss owing to mass gain/loss per time.

3.3.2. Evaporation

The evaporation rate m'' is obtained following Sikanen and Hostikka [16], which treated $X_{\mathrm{fu,equil}}$ as a function of $T_{\mathrm{liq,Inter}}$ and T_{b} based on the Clausius-Clapeyron relation:

$$X_{\mathrm{fu,equil}}=\exp\left[-\frac{h_{\mathrm{vap}}M_{\mathrm{fu}}}{R}\left(\frac{1}{T_{\mathrm{liq,Inter}}}-\frac{1}{T_{\mathrm{b}}}\right)\right] \tag{11}$$

where $T_{\mathrm{liq,Inter}} = T_{\mathrm{liq,First}}$ as heat balance is considered in the first cell next to the interface. This treatment will be discussed in Section 3.3.3. The local mass burning rate m'' can be obtained by Stefan diffusion:

$$m'' = h_{\mathrm{mass}} \frac{\bar{p}_{\mathrm{First}} M_{\mathrm{fu}}}{R T_{\mathrm{First}}} \ln\left(\frac{X_{\mathrm{fu,First}} - 1}{X_{\mathrm{fu,equil}} - 1} \right) \qquad \mathrm{kg/(s{\cdot}m^2)}, \text{ and} \tag{12}$$

$$m''' = \frac{m'' S_{\mathrm{Inter}}}{V_{\mathrm{First}}} \qquad \mathrm{kg/(s{\cdot}m^3)}, \tag{13}$$

Since heat balance is considered in the first cell in this model, m'' is converted to mass burning rate per volume m''' through Eq. (13). Sikanen and Hostikka assumed that diffusion of vaporised fuel via a stagnant film influence m''. However, a thickness of the stagnant film δ_{film} cannot be defined in the simulation, and it is hence determined by a mass transfer correlation:

$$h_{\mathrm{mass}} = \frac{D_{\mathrm{vap,gas}}}{\delta_{\mathrm{film}}} = \frac{Sh D_{\mathrm{vap,gas}}}{L} \qquad \mathrm{m/s}, \text{ and} \tag{14}$$

$$D_{\mathrm{vap,gas}} = \frac{\mu}{\bar{\rho} Sc} \qquad \mathrm{m^2/s}, \tag{15}$$

where Sc = 0.6 [16]. $D_{\mathrm{vap,gas}}$ is the binary diffusion coefficient between a fuel vapor and gas; Sh is given as [36]:

$$Sh = 0.664 Sc^{1/3} Re^{1/2} \qquad Re < 5.0 \times 10^5, \tag{16}$$

Sh is evaluated using field variables at the cell centre in the first cell , $Re = \bar{\rho} |\mathbf{u}| L / \mu$, and $\mathbf{u}$ is the velocity vector (m/s). Sikanen and Hostikka [16] calculated Sh for $Re > 5.0 \times 10^5$. However, in the present study, Re is typically < 100, hence Eq. (16) is used. L is estimated following Beji et al.[29]:

$$L = \frac{\pi r^2}{2\pi r} \qquad \mathrm{m}, \tag{17}$$

The interface velocities in the normal direction $u_{\mathrm{n,Inter}}$ and $u_{\mathrm{n,liq,Inter}}$ are obtained from m'' in Eq. (12). Momentum in the normal direction at the interface is exchanged as follow:

$$u_{\mathrm{n,liq,Inter}} = \frac{m''}{\rho_{\mathrm{liq}}} \qquad \mathrm{m/s} \text{ for the liquid phase, and} \tag{18}$$

$$u_{\mathrm{n,Inter}} = \frac{m''}{\bar{\rho}} \qquad \text{m/s for the gas phase,} \tag{19}$$

Equation (19) is effectively the inlet condition for the gas phase, whereas Eq. (18) is the outflow condition for the liquid phase.

3.3.3. Sensible enthalpy balance near the interface

Following previous evaporation models [14–16,27], it is assumed that evaporation occurs very near the interface. The assumption is valid if the bubbling layer near the interface is very thin. Heat balance is considered in the first cell which corresponds to the bubbling layer. This treatment facilitates the inclusion of heat transfer from the container side wall and near the surface in the evaporation calculation. It also prevents infinite m'' if heat flux at the interface is very high, which could occur close to the rim, which causes very low liquid temperature near the wall.

The interface conditions for sensible enthalpy are calculated as:

$$-\lambda_{\mathrm{liq}} \frac{\partial T_{\mathrm{liq}}}{\partial x_j} = q''_{\mathrm{conv}} - \varepsilon_{\mathrm{rad,liq}} \sigma_{\mathrm{Boltz}} T^4_{\mathrm{liq,Inter}} \text{ for the liquid phase, and} \tag{20}$$

$$T_{\mathrm{Inter}} = T_{\mathrm{liq,Inter}} \qquad \text{for the gas phase} \tag{21}$$

where q''_{rad}, $m''h_{\mathrm{vap}}$, and $m''h_{\mathrm{liq}}$ do not appear in Eq. (20). Since radiative heat flux is computed based on Beer's law, its effect does not appear in Eq. (20), and only surface emission at the interface is considered by the second term on the right side. In-depth radiation will be explained in Section 3.3.7. $m''h_{\mathrm{vap}}$ is expressed as the source term in Eq. (9). Since the effect of $m''h_{\mathrm{liq}}$ is given by an outflow condition of the momentum equation, it can be ignored in Eq. (20). Above balanced heat in the first cell transfers from the top to pool bottom as denoted as (l) in Fig. 1.

q''_{conv} is given as

$$q''_{\mathrm{conv}} = \lambda_{\mathrm{Inter}} \frac{(T_{\mathrm{First}} - T_{\mathrm{Inter}})}{\Delta_{\mathrm{First}} / 2} \qquad \mathrm{W/m^2}, \tag{22}$$

where Δ_{First} is the first cell along the interface.

Since the gas phase properties are sensitive to the temperature and concentrations of the chemical species, multi components formulation is used at the interface. λ_{Inter} is given following [28]:

$$\lambda_{\text{Inter}} = \sum_{I} \frac{\lambda_I}{1 + \sum_{K \neq I} X_K \cdot 1.065 \Phi_{IK}} \quad \text{W/(m·K), and} \tag{23}$$

The correction factor Φ_{IK} is calculated as:

$$\Phi_{IK} = \frac{1}{2\sqrt{2}} \left(1 + \frac{M_I}{M_K}\right)^{-\frac{1}{2}} \left[1 + \left(\frac{\mu_I}{\mu_K}\right)^{\frac{1}{2}} \left(\frac{M_K}{M_I}\right)^{\frac{1}{4}}\right]^2, \tag{24}$$

The species *I* and *K* at the interface considered only fuel vapor and gas and the fuel vapour is treated separately from the gas. μ and λ of the gas are obtained by the Sutherland equation [9,11], the modified Eucken correlation [31] and *M* of the gas is estimated as a mean molecular weight. Several properties of the fuel vapor for methanol, ethanol, heptane and acetone can be obtained from references [29,38]. At the interface, the concentration is assumed to be the equilibrium state; the gas and fuel vapour volume fractions are given as

$$X_{\text{fu,vap}} = X_{\text{fu,equil}}, \text{ and} \tag{25}$$

$$X_{\text{gas}} = 1 - X_{\text{fu,vap}}, \tag{26}$$

where $X_{\text{fu,equil}}$ indicates a fuel vapor at the equilibrium state.

3.3.4. Shear stress balance near the interface

Momentum exchange between the gas and liquid phases occurs at the interface. The interface velocities in the tangential direction for the gas and liquid phases are given based on continuity of shear stress balance [27] between the gas and liquid phases as denoted as (g) in Fig. 1. The liquid interface velocity in the tangential direction $\mathbf{u}_{\text{liq,Inter,tan}}$ is given by solving following equation:

$$\mu_{\text{Inter}} \frac{\mathbf{u}_{\text{First,tan}} - \mathbf{u}_{\text{liq,Inter,tan}}}{\Delta_{\text{First}} / 2} = \mu_{\text{liq,Inter}} \frac{\mathbf{u}_{\text{liq,Inter,tan}} - \mathbf{u}_{\text{liq,First,tan}}}{\Delta_{\text{First,liq}} / 2} - \frac{\nabla_{\tan}\sigma_{\text{Mar}}}{\Delta_{\text{liq,First}}} \quad \text{for the liquid phase} \tag{27}$$

The gas phase interface velocity in the tangential direction $\mathbf{u}_{\text{Inter,tan}}$ is given as

$$\mathbf{u}_{\text{Inter,tan}} = \mathbf{u}_{\text{liq,Inter,tan}} \quad \text{for the gas phase} \tag{28}$$

where $\nabla_{\tan}$ is the derivative in the tangential direction. This treatment allows to interact convection and diffusion. μ_{Inter} in Eq. (27) is given by [28]:

$$\mu_{\text{Inter}} = \sum_{I} \frac{\mu_I}{1 + \sum_{K \neq I} \frac{X_K}{X_I} \Phi_{IK}} \quad \text{kg·m/s,} \tag{29}$$

where the procedure of Eq. (27) is the same as Eqs. (23) and (24).

3.3.5. Side wall condition

For simplicity, the measured conductive heat transfer from the container wall to the liquid fuel q''_{sidewall} is used as the boundary condition. The boundary condition for the sensible enthalpy of the liquid phase at the side wall is given as

$$-\lambda_{\text{liq}} \frac{\partial T_{\text{liq}}}{\partial x_j} = \frac{T_{\text{wall}} - T_{\text{liq,wall}}}{\Delta r / \lambda_{\text{wall,solid}} + \Delta r / \lambda_{\text{wall,liq}}} \quad j = 2 \text{ and } 3 \ (y \text{ and } z \text{ directions}) \quad \text{W/m}^2, \tag{30}$$

where $T_{\text{wall,solid}}$ is the measured wall temperature obtained from reference [17], $T_{\text{wall,liq}}$ is obtained by the predicted temperature on the wall, $\Delta r = 5 \times 10^{-4}$ m [17], $\lambda_{\text{wall,solid}} = 1400$ W/m/K for quartz and $\lambda_{\text{wall,liq}}$ are estimated on the wall, which is assumed as non-slip.

3.3.6. Pool bottom condition

The liquid temperature near the container bottom is assumed to be the same as T_{bot}:

$$T_{\text{liq}} = T_{\text{bot}} \quad \text{K} \tag{31}$$

The mass flow rate $\dot{m}$ is the same as the mass burning rate given at the pool bottom for the momentum condition in the following the experiment [3], assuring mass conservation in the pool as:

$$\dot{m}_{\mathrm{x}} = m'' S_{\mathrm{Inter}} \quad \mathrm{kg/s} \tag{32}$$

3.3.7. In-depth radiation

Following our previous study [19], q''_{rad} is computed by Beer's law, neglecting emission inside the pool [19]:

$$q''_{\mathrm{liq,rad}} = \eta_{\mathrm{rad,liq}} q''_{\mathrm{rad}} \exp(-a_{\mathrm{rad,liq}} \Delta_{\mathrm{dep}}) \quad \mathrm{W/m^2}, \tag{33}$$

where $q''_{\mathrm{liq,rad}}$ decreases with increasing Δ_{dep} because $q''_{\mathrm{liq,rad}}$ is absorbed in liquid fuel.

3.4. Model parameters and physical properties

Unlike previous studies [14,15,29] which assumed the liquid properties to be constant, they are calculated as a function of T as plotted in Fig. 4 [38]. λ_{vap} and μ_{vap} are used in Eqs. (23) and (24).

$Le_{\mathrm{O_2}}$ = 1.11 [32], $Le_{\mathrm{H_2O}}$ = 0.83 [32], $Le_{\mathrm{CO_2}}$ = 1.39 [32], $Le_{\mathrm{N_2}}$ = 1.0 [32], $Le_{\mathrm{CH_3OH}}$ = 1.31 and $Le_{\mathrm{C_2H_5OH}}$ = 1.72, where the Lewis numbers of methanol and ethanol were estimated following Fuller et al. [39].

3.5. Numerical conditions

The second order central linear scheme is used for the momentum equations and the central linear scheme limited by total variation diminishing (TVD) is used for the governing equations of the mass fraction of chemical species and the energy equation of the gas phase. The central linear scheme is applied to all the equations for liquid phase. The second order backward differential scheme was chosen for time marching. The outer iteration and number of the pressure correction were set to 7 and 2 for the gas phase simulation, respectively, while 3 and 2 for liquid phase simulation. For gas phase combustion, the irreversible one step chemistry model is used:

$$\mathrm{C}_x\mathrm{H}_y\mathrm{O}_z + (x + y/4 - z/2)\mathrm{O}_2 \rightarrow x\mathrm{CO}_2 + \frac{1}{2} y\mathrm{H}_2\mathrm{O}. \tag{34}$$

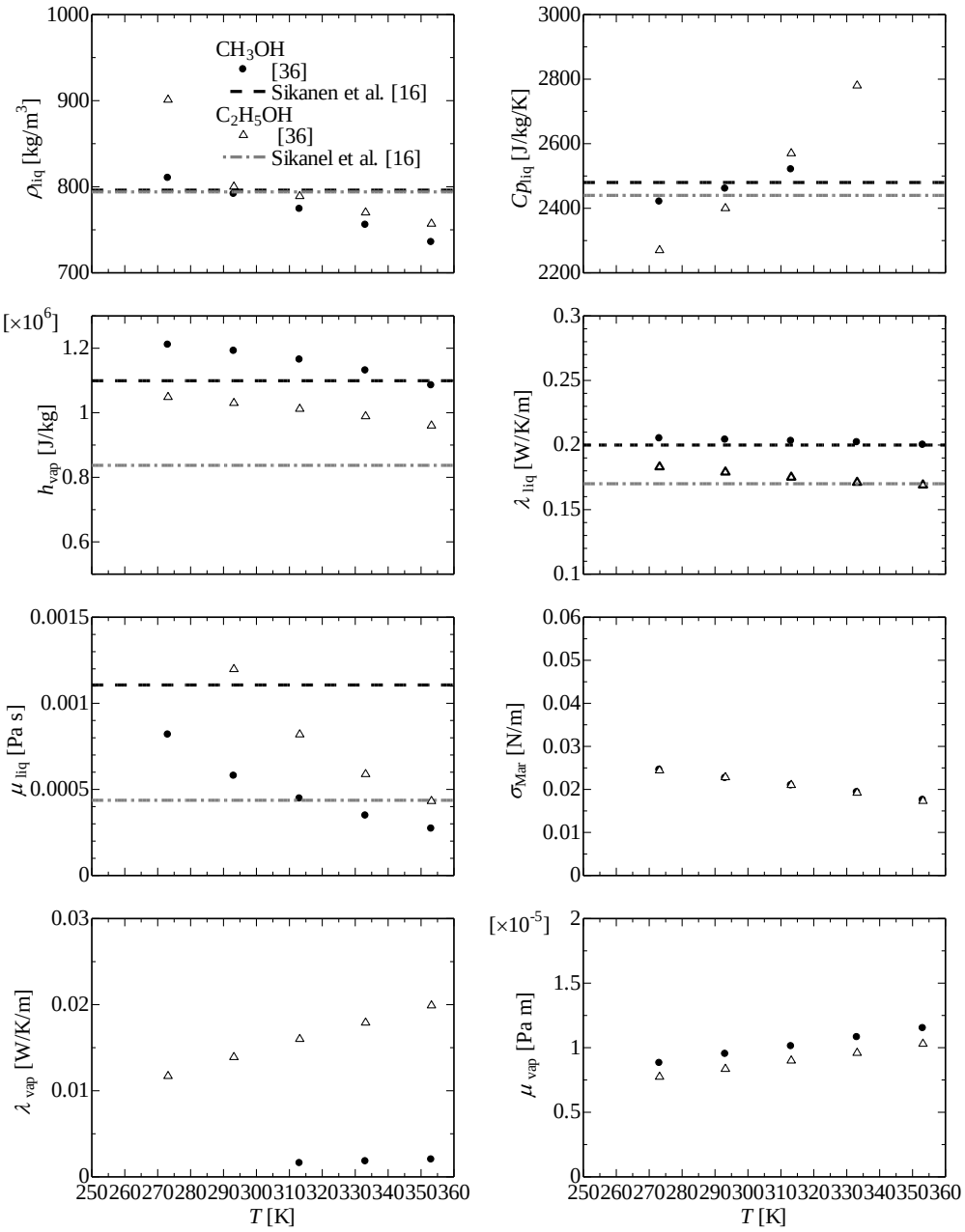

Fig. 4 Properties of methanol and ethanol [38].

Comparison was made the measurements of Vali et al. [3]. In the experiment, a circular burner was made of quartz with an inner diameter = 90 mm ($2r$), outer diameter = 95 mm and height (pool depth d) = 12 mm. The container was filled with methanol and the fuel was refilled continuously to make sure that the surface height was equal to the rim height so the lip height was zero.

Table. 1 Input parameters for simulations.

Parameters	Values
Pr_t and Sc_t	0.85
$a_{rad,liq}$	1140 [1/m] [16]
$\varepsilon_{rad,liq}$	0.95 [29]
$r_{rad,liq}$	0.02 (= water's value)
$\eta_{rad,liq}$	0.98 (1- $r_{rad,liq}$)
T_b for methanol	337.85 K [38]
T_b for ethanol	351.45 K [38]
R_o for methanol	0.7 (numerical calibration)
R_o for ethanol	0.85 (numerical calibration)

4. Results

4.1. Gas phase simulation

The computational domain for the gas phase is shown in Fig. 5. The respective dimensions are x_{max} = 0.6 m, y_{max} = z_{max} = 0.27 m, r = 0.045 and δ = 0.0025 m; the coordinate origin (0, 0, 0) was set at the pool centre on the surface. $\dot{m}$ = 5.9×10^{-5} kg/s, the temperature at the interface was T = 337.85 K and temperature at the rim was $T \approx$ 385 K, where the values of $\dot{m}$ and temperature at the rim were obtained from the experiment for T_{bot} = 268.15 K [3,17].

Two computational grids were considered to check grid sensitivity. The initial number of cells across the pool diameter was 32; then the first grid layer was locally subdivided in all the directions,

resulting in 64 cells on the pool surface. In the y and z directions, the cell size was reduced to Δr_{rim} = 0.751 mm close to the rim. The first grid size from the interface Δx_{First} was 0.5 mm with the expansion ratio ≈ 3–4% and a total of 228,288 cells. For a finer computational grid, the number of cells in each direction was increased by 25%; as a result, a total of 448,500 cells were used.

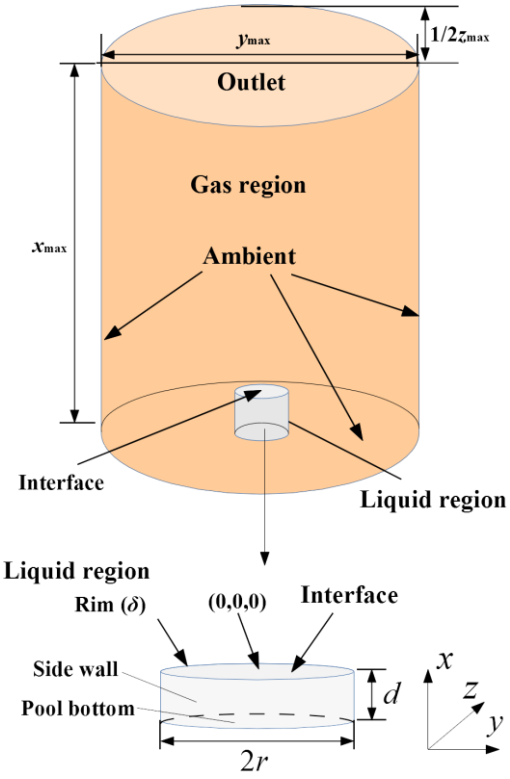

Fig. 5 Sketch of the computational domain.

Figure 6 shows (a) $u_x/q^{2/5}$, (b) ΔT , (c) flame height x_f and (d) heat fluxes predicted at different grid resolutions, where ΔT is calculated as $\Delta T = T - 293.15$, $q = \Delta h_{comb} \times \dot{m}''$ and x_f is given by the highest location with the stoichiometric mixture fraction following previous studies [7,19]. $q''_{net} = q''_{tot} - q''_{re}$, and q''_{re} is the absolute value of re-radiative heat flux. The differences in the predicted x_f, $u_x/q^{2/5}$ and heat fluxes are small, whereas ΔT is slightly different. Since the predicted x_f at different resolutions are similar, 228,288 cells are used in following sections.

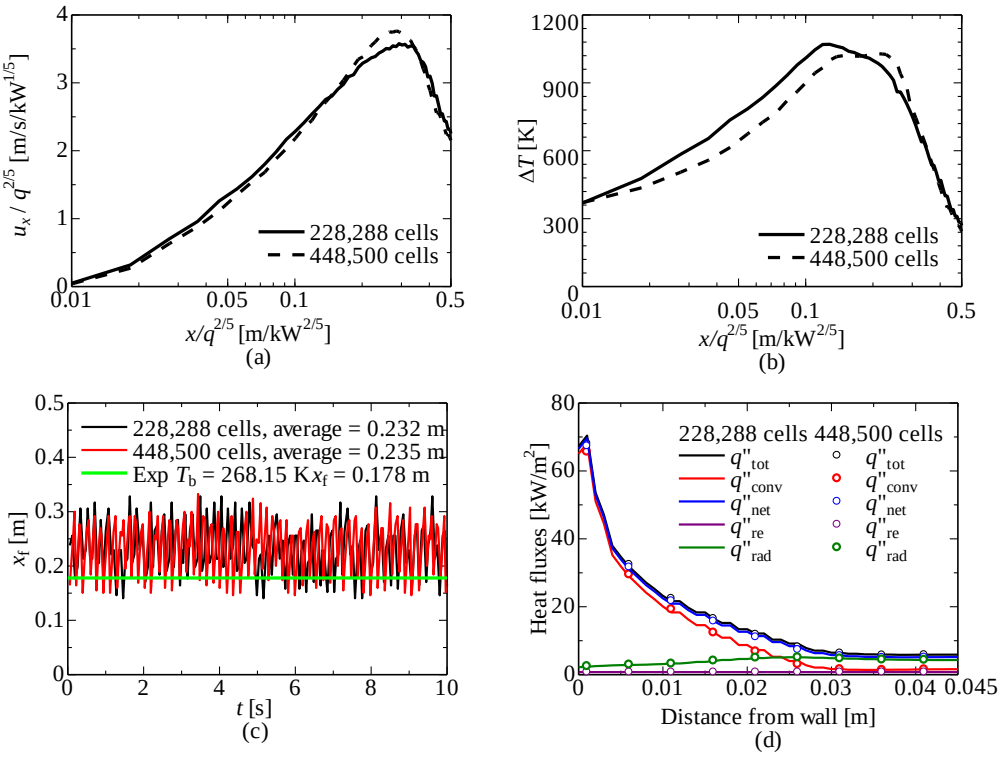

Fig. 6 (a) *Ux*, (b) ΔT, (c) flame height x_f and (d) heat fluxes with different grid resolutions.

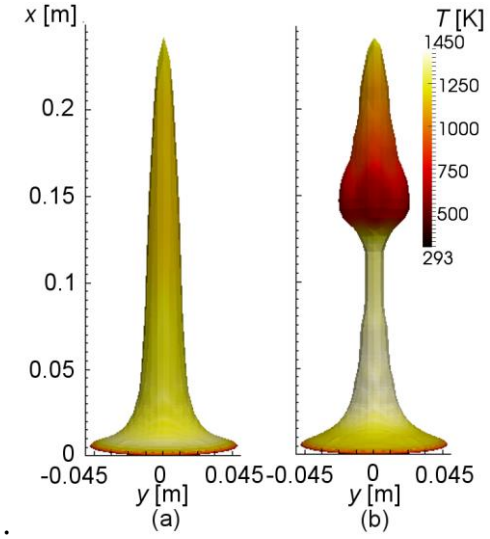

Fig. 7 (a) Mean and (b) instantaneous flame volumes defined as $0 \leq R_o \leq 0.7$

Figure 7 shows the predicted flame volume, which is defined as $0 \leq R_o \leq 0.7$ based on accordance between the flame height and tip of flame volume as confirmed in Fig. 6. The instantaneous flame shape is like the mushroom-cap shape experimentally observed by Hayasaka [41].

4.2. Grid sensitivity test for liquid phase simulation

A gas-liquid coupled simulation was also conducted to test grid sensitivity. The respective dimensions in Fig. 5 were: x_{max} = 1.0 m, y_{max} = z_{max} = 0.405 m, d = 0.012 m, r = 0.045, and δ = 0.0025 m. The computational domain was extended to prevent a backflow owing to numerical instability. A total of 533,952 cells were used for the gas phase with about 3% expansion ratio. In the liquid region, divisions in the x direction were changed to 26, 40, and 57 with the expansion ratio of 3%; the respective first Δx were 0.15 mm, 0.301 mm and 0.0751 mm. Δy and Δz were the same as the gas phase sizes. The measured temperature was used as an initial condition. The data were extracted after the predicted m'' was confirmed to be under quasi steady state.

Figure 8 depicts the predicted distribution of T and velocity vector fields with different grid resolutions in the liquid phase. The predicted total mass burning rates $\dot{m}$ in cases (a)–(c) in Fig. 8 are 6.0699 × 10^{-5}, 6.1488 × 10^{-5} and 6.3602 × 10^{-5} kg/s. Hence, although the grid resolution slightly affects $\dot{m}$, the difference in $\dot{m}$ between cases (a) and (b) is only about 1.3%, hence the resolution in (b) is considered to be sufficiently accurate.

Two vortices are observed in the predictions for cases (a) and (b) but not in case (c) which had the least grid resolution. Hereafter, the left vortex is referred to as the first vortex and the right side one as the second vortex. There is no obvious difference between the predictions for cases (a) and (b) except the interface velocity near the second vortex. The resolution in case (a) is used for better accuracy in the subsequent calculations.

Two further cases were simulated to test grid sensitivity of the first grid height from the interface in the gas phase, which is Δ_{First} in Eq. (22). Equation (22) would be valid if the boundary layer is well resolved. Δ_{First} = 0.421, 0.25 and 0.15 mm were prepared, and $\dot{m}$ is plotted in Fig. 9. A difference in $\dot{m}$ between Δ_{First} = 0.421 and 0.25 mm seems to be large, but its error is 1.5%. The predicted $\dot{m}$

with Δ_{First} = 0.25 and 0.15 mm are almost similar and therefore, $\Delta x_{First,gas}$ = 0.25 mm are used in following sections.

Determined sizes are: $\Delta x_{First,liq}$ = 0.0715, $\Delta x_{First,gas}$ = 0.25, $\Delta y_{liq,gas,min}$ = 0.377 and $\Delta y_{liq,gas,min}$ = 0.95 mm with a total of 569,088 cells.

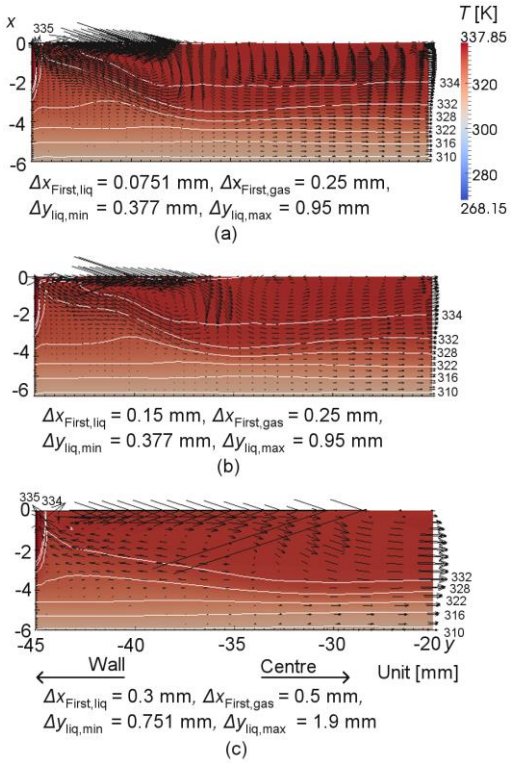

Fig. 8 Predicted distributions of temperature and velocity vectors with different grid resolutions.

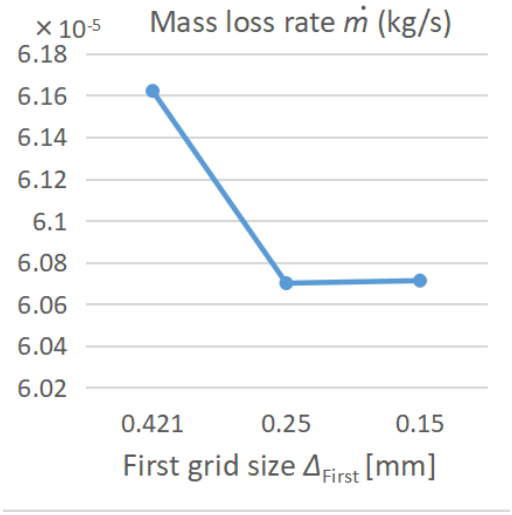

Fig. 9 Dependency on the first grid size from the interface.

4.3. Validation of gas-liquid approach

Further simulations were performed for validation of the gas-liquid approach. The dimensions in Fig. 5 are the same as section 4.2. Cases with varying container bottom temperature T_{bot} were simulated: 268.15, 280.15, 297.15 and 313.15 K. The temperatures at the rim and $T_{wall,solid}$ in Eq. (30) were set to 385, 388, 393 and 398 K for each case as measured in [17]. The simulations were continued until reaching the steady $\dot{m}''$.

Figure 10 shows $\dot{m}$ *vs* T_{bot}. $\dot{m}$ increases with increasing T_{bot}. The increase of T_{bot} would lead to higher surface temperature. The predicted total mass burning rates are within 3% of the measurements for all the cases.

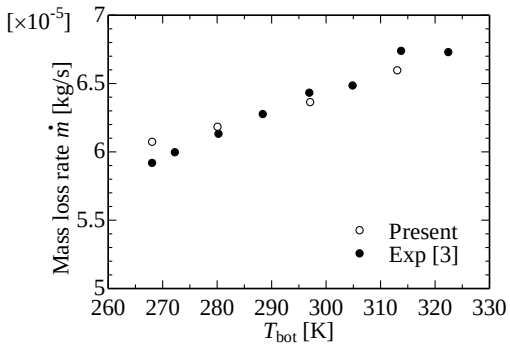

Fig. 10 Comparison between the predicted and measured total mass burning rate *vs* fuel temperature at the container bottom.

The predicted and measured flame height x_f *vs* the temperature at the container bottom T_{bot} are shown in Fig. 11. The flame height is slightly overpredicted by ???%. Since a change in $\dot{m}$ is small, a trend in x_f is not clear. The predicted x_f is approximately between 0.24 to 0.25 m. The predicted and measured x_f *vs* $\dot{m}$ is presented in Fig. 12, where McCaffrey's correlation [10] is plotted as reference. The predictions are slightly overestimated compared with the measurements and McCaffray's correlation, but the discrepancy is within ???%.

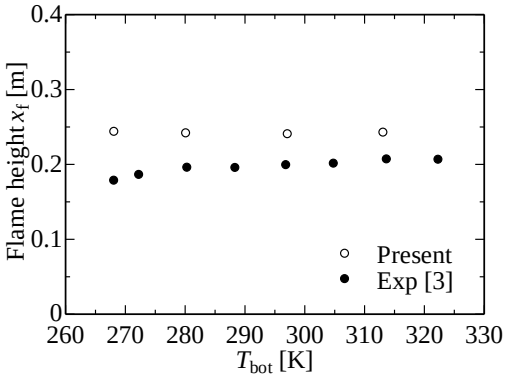

Fig. 11 Predicted and measured flame height *vs* fuel temperature at the container bottom.

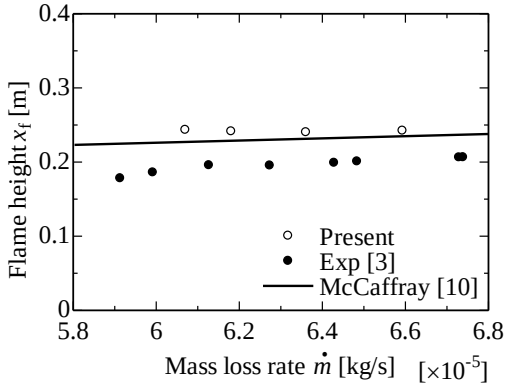

Fig. 12 Predicted and measured flame height *vs* mass burning rate.

In Fig. 13, the dimensionless T^* *vs* dimensionless depth is presented, where T^* is calculated as $T^* = (T_{liq} - T_{bot})/(T_{Inter} - T_{bot})$ and x^* is calculated as $x^* = 1 + x/d$. The predictions are in reasonably good agreement with the measurements in most cases except for T_{bot} = 313.15 K where relatively large discrepancy of around 20% is seen for $x^* > 0.5$. The changing trends of the predicted T^* are similar, namely, it increases almost linearly with x^* until x^*= 0–0.6 or 0.7, and remains almost constant thereafter. It is noted that the changing trend of the measured T^* was different from the others, i.e. it increases continuously but the reason for this was not clear [3].

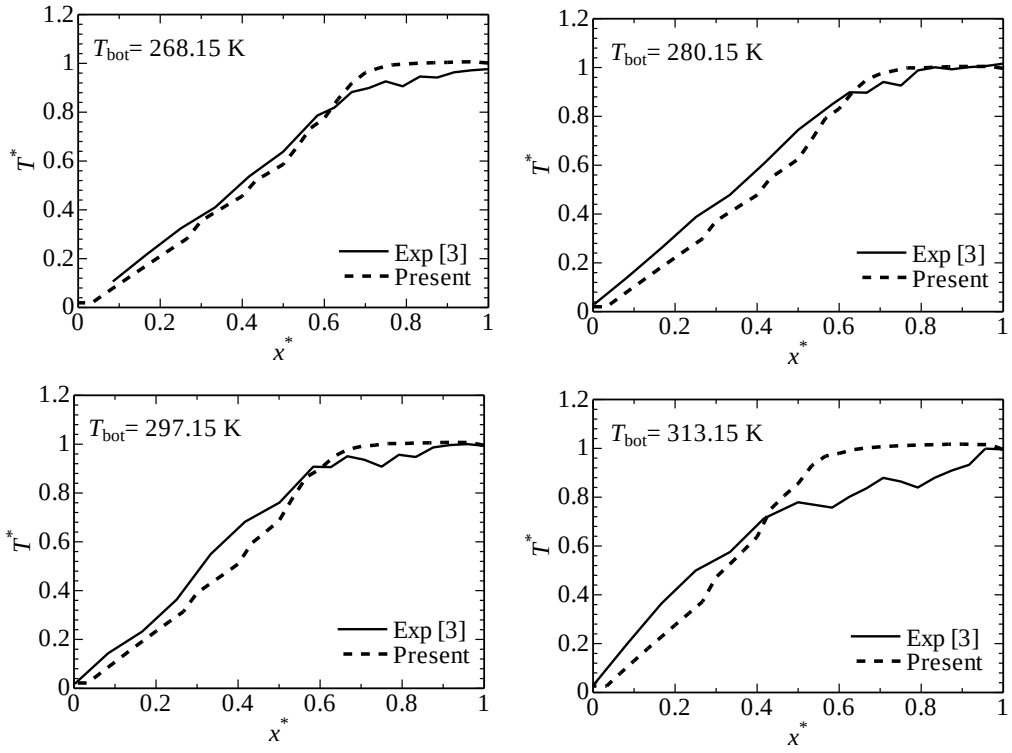

Fig. 13 Predicted and measured dimensionless temperature T^* *vs* dimensionless depth along the centreline.

Figure 14 (a) and (b) shot that the differences between the predicted and measured heat fluxes and m'' for T_{bot} = 268.15–313.15 K are very small while the predicted m'' close to the wall are slightly different. As the total heat flux *vs* burning rate was not measured by Vali et al. [3], different experimental data is used for discussion. Singh and Gollner [40] conducted tests with a porous non-combustible material soaked with fuels; they measured the local heat fluxes and m'' in the vertical laminar boundary layers of methanol and ethanol. It is currently difficult to simulate their configurations because of a lack of necessary information of the porous media such as heat conductivity, density and heat capacity. Assuming the local mass burning rate m'' is a function of the local q''_{tot}, their data can be considered as comparable with the present scenarios. However, a minor difference in m'' owing to a difference in rear side temperature (equal to a difference in T_{bot}) is observed. Figure 14 (c) shows the predicted and measured m'' *vs* q''_{tot} are in reasonably good

agreement. A decrease in T_{bot} slightly reduces m'', especially at higher q''_{tot}. A difference in m'' between T_{bot} = 268.15–313.15 K is due to $m''h$ from the rear side as stated above. Additionally, the predicted m'' at the wall does not follow a trend in m'' *vs* q''_{tot}. At the wall, q''_{tot} and $q''_{sidewall}$ affect m'', and the predicted data are not comparable. Fig. 14 (d) shows m'' *vs* q''_{tot} for ethanol with T_{bot} = 297.15 K. Although the main focus here is the methanol pool fire, an additional simulation was conducted for the ethanol case using the properties in Fig. 1 as well to facilitate comparison which again demonstrates reasonably good agreement.

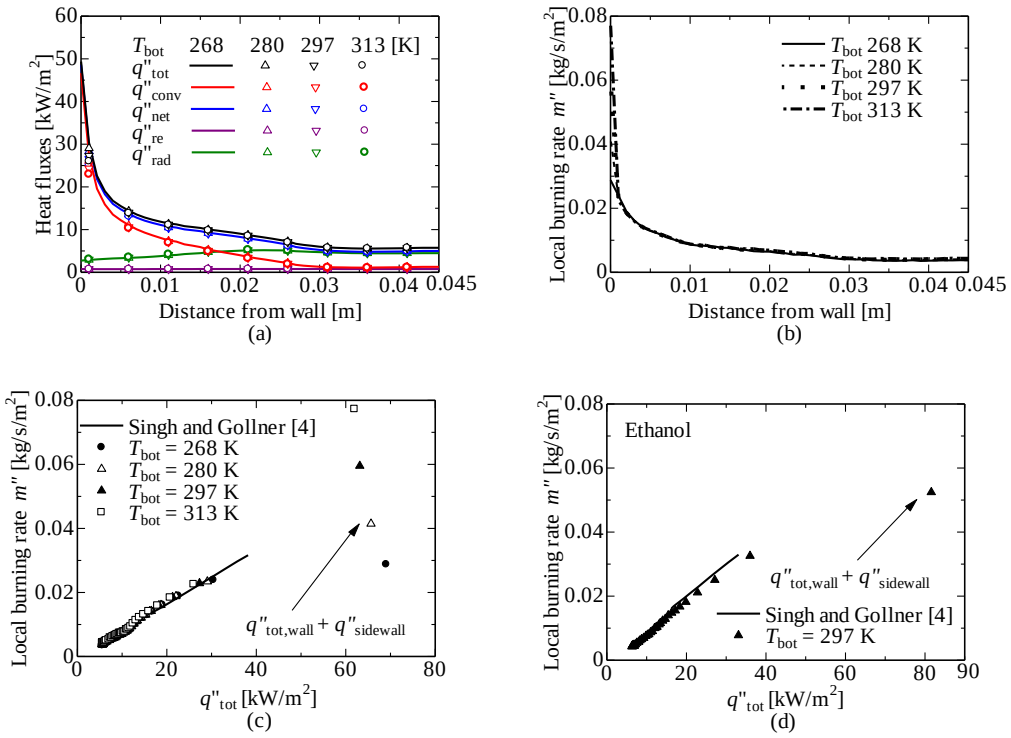

Fig. 14 Predicted local (a) heat fluxes, (b) local burning rate m'' *vs* distance from the wall, (c) local burning rate m'' *vs* total heat flux and (d) local burning rate m'' *vs* total heat flux for ethanol.

4.4. Analysis of the liquid phase

Figure 15 depicts the distributions of T_{liq}, where it should be noted that x is the vertical direction and y is the horizontal direction. As shown in Fig. 15, a temperature gradient is smaller for T_{bot} = 313.15 K; it causes a small heat loss from the pool bottom, resulting in the large m'' owing to the

high surface temperature. The highest surface temperatures are predicted just near the rim owing to q''_{cond} from the wall; the relatively lower surface temperatures appear at $-40 < y < -35$ mm and the surface temperatures become higher at $-30 < y < -25$ mm. The non-uniform temperature distribution is due to a difference in the distributions of q''_{conv} and q''_{rad} as observed from Fig. 14, i.e. the peak q''_{conv} is predicted near the wall, whereas the peak q''_{rad} occurs approximately around the middle coordinate between the wall and pool centre. Also, at $-30 < y < -25$ mm inside the pool, the slightly higher temperature regions are observed because q''_{rad} heats the liquid fuel owing to in-depth radiation in Eq. (33).

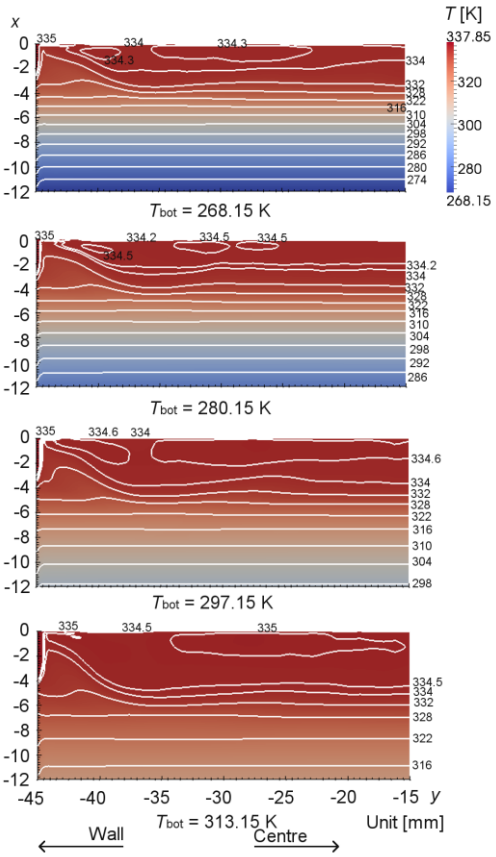

Fig. 15 Predicted distributions of T_{liq} and velocity vector fields in the liquid phase.

Figure 16 shows the predicted velocity vector fields in the liquid phase with the velocity magnitude defined as $(u_{x,\text{liq}}{}^2 + u_{y,\text{liq}}{}^2)^{0.5}$. The two vortices are seen near the wall and their sizes

increase with increasing T_{bot}. This is inline with the experimental observation of Vali et al. [3]. μ_{liq} decreases as T_{liq} increases as shown in Fig. 4. If the Reynolds number is defined as $Re = u_{liq,Inter} \cdot r/\mu_{liq}$, the effect of inertia in the pool is stronger as T_{liq} increases. The effect of decreasing μ_{liq} is hence similar to that of increasing $u_{liq,Inter}$.

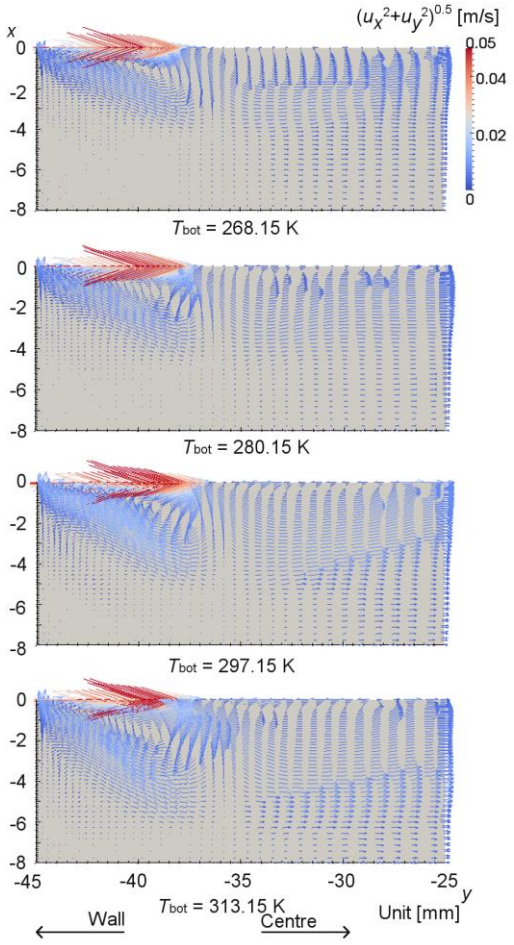

Fig. 16 Predicted velocity vectors in the liquid phase.

Relatively large velocities owing to thermocapillary is found near the wall. The interface velocity above the first vortex centre is 0.0224 m/s for T_{bot} = 268.15 K and 0.0219 m/s for T_{bot} = 313.15 K. The velocity magnitude were not measured in [3] but the authors later reported approximately 0.02 m/s for T_{bot} = 311.15 K and d = 18 mm above the first vortex centre in subsequent work [42]. It should be noted that the vortex position changed with T_{bot} in the experiment. This was not captured in the present simulations. A possible explanation is that the predicted liquid temperature is not

sufficiently precise to capture a change in the location. As shown in Fig. 14, a trend in m'' *vs* q''_{tot} is very different close to the wall; it causes the high temperature there, leading to a strong flow owing to thermocapillary force. Therefore, the first vortex position is moved toward the pool centre direction. The mechanisms of the two vortices will be discussed later with Fig. .

Figure 17 shows the predicted (a) gas and liquid temperatures and (b) velocity vector fields near the interface for T_{bot} = 297.15 K. The vector lengths are very different in the liquid and gas phases owing to the very different magnitudes. In Fig. 17 (a), high temperature is observed near the wall, and the distance between the flame and interface (termed a standoff distance) is shorter close to the wall. Thus, q''_{conv} and q''_{tot} are very high near the wall as shown in Fig. 14, with the high temperature and short standoff distance. Near the wall, a strong gas flow toward the flame is observed in Fig. 17, dragging a liquid toward the pool centre owing to shear stress in the pool. However, a gas flow from the pool centre to wall is not seen in Fig. 17, which was assumed to be a reason behind the appearance of the second vortex suggested by Vali et al. [3].

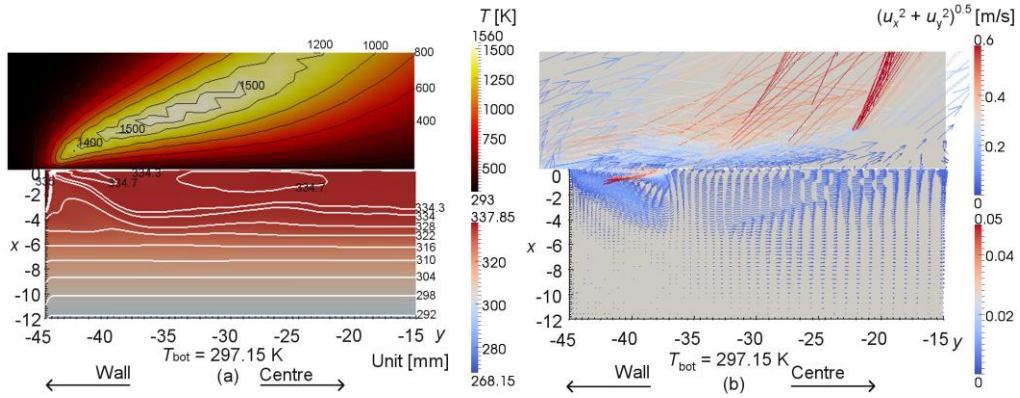

Fig. 17 Predicted (a) gas and liquid temperatures and (b) velocity vector fields near the interface for T_{bot} = 297.15 K.

Figure depicts the predicted temperature and velocity vectors near the two vortices for T_{bot} = 313.15 K with bounded T_{liq} for 333–336 K. A somewhat large difference in the temperature is observed just near the wall, resulting in a flow toward the pool centre because of thermocapillaly force. Furthermore, a very small difference in T_{liq} is observed between the first and second vortices.

Owing to low temperature here, a liquid flow moves from the pool centre to wall owing to thermocapillaly force, as well as from the wall to pool centre. Namely, shear stress and thermocapillary force cause a flow from the wall to centre, and the one from the pool centre to wall is triggered by thermocapillary force. The two flow streams collide at the low temperature region, resulting in a downward flow which splits into one stream toward the wall and the other toward the pool centre.

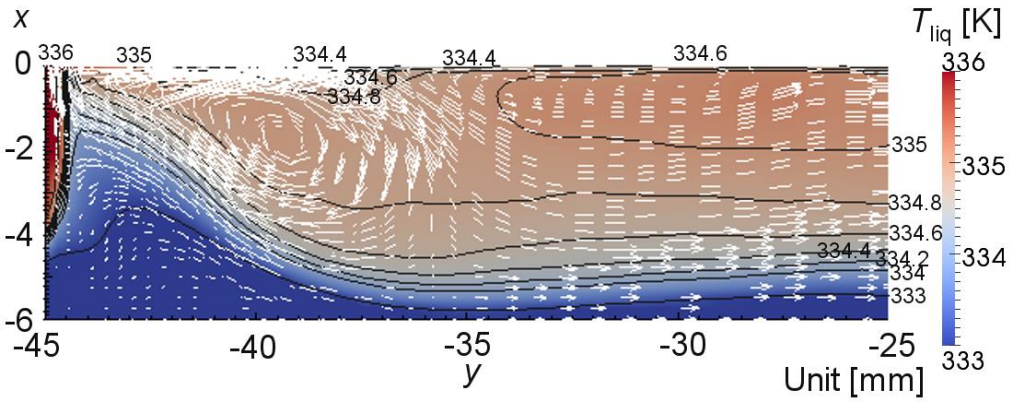

Fig. 18 Predicted temperature with velocity vector fields close to two vortices for T_{bot} = 313.15 K, where T_{liq} is bounded for 333–336 K.

In addition, a relatively large amount of evaporation occurs owing to high q''_{tot} and $q''_{sidewall}$ near the container wall. As liquid fuel was continuously supplied to keep a surface height level, that is expressed via an outflow condition in the gas-liquid approach as discussed in Eq. (20). For T_{bot} = 297.15 K, $u_{n,Inter}$ = 7.9170 × 10^{-5} m/s near the rim is obtained by Eq. (18), where m'' = 0.059536 kg/m^2 and ρ_{liq} = 752 kg/m^3 are obtained from Figs. 4 and 14; thus, the effect of evaporation is not larger than that of shear stress and thermocapillary.

Figure 19 summarizes the overview of the flow mechanisms in the small pool. A small difference in the temperature between the vortices was not discussed in Vali et al.'s experiment [3], but it was seen in the case of T_{bot} = 313.15 K. More distinct differences were observed in further investigation of Vali et al. in their later study [44].

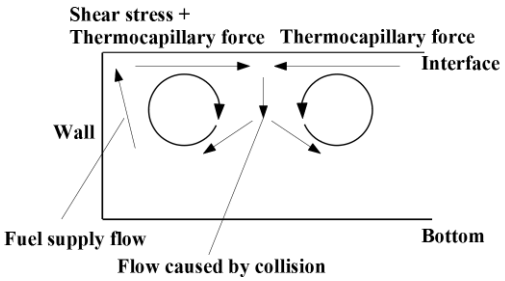

Fig. 19 Overview of flow mechanisms.

4.5. Gas-liquid phases' interaction

Figure 20 (a) shows the predicted x_f and $\dot{m}$ *vs t*, where (a)–(e) are also used for following Fig. 21. One cycle of oscillations of $\dot{m}$ and x_f is found to be similar, which is approximately 0.18 s corresponding to (a)–(f). Their trends are slightly different, i.e. x_f falls abruptly from (e)–(f), whereas such a change in *m* is not observed in Fig. 20 (a).

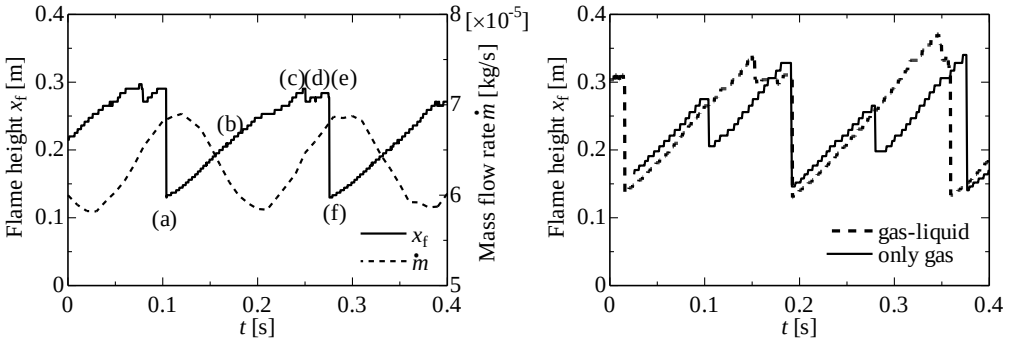

Fig. 20 Predicted (left) x_f and $\dot{m}$ *vs t* for T_{bot} = 297.15 K and (right) comparison of predicted x_f vs time using different approaches for T_{bot} = 268.15 K.

As shown in Eqs. (12) and (11), m'' is a function of $T_{liq,Inter}$; m'' varies in accordance with time, meaning that $T_{liq,Inter}$ also changes depending on time. A major contribution of heat transfer is q''_{conv}, followed by q''_{rad} mainly owing to a flame; therefore a flame motion such as x_f in Fig. 20 is thought to be important for m''. Further, in Fig. 20 (b), a minor difference in x_f is found between the coupled and decoupled approaches, but one cycle period is similar, i.e. oscillation of $\dot{m}$ is not important for a trend in x_f. Therefore, oscillation of $\dot{m}$ can be attributed to a flame motion.

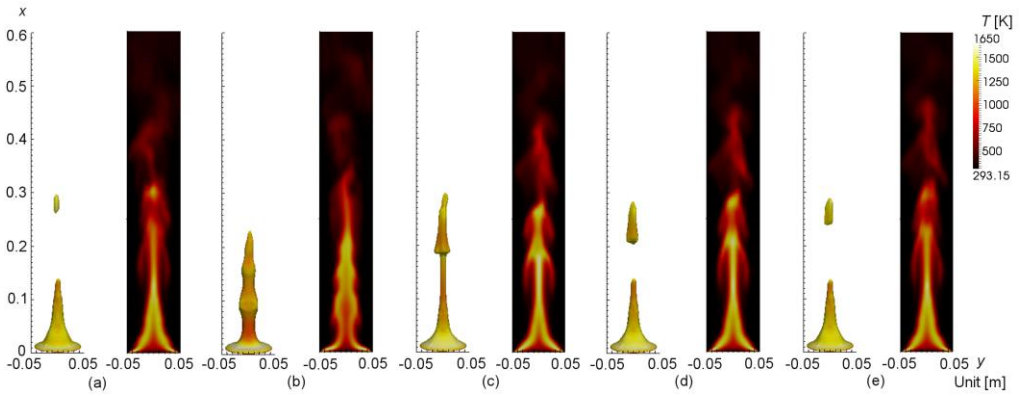

Fig. 21 Predicted transient flame volume and distribution of T for T_{bot} = 297.15 K.

Figure 21 shows the predicted flame volume and temperature distribution between phases (a)–(e). In phase (a), the predicted x_f is the shortest, and a flame shape is similar to a 'cone'. In phase (b), the flame near the pool surface becomes thinner than that in the phase (a) and the necking phenomena is observed. In the phase (c), a mushroom cap shape appears with the highest x_f. After the flame reaches the highest point, (d) the flame is divided into tip and base parts. The former disappears owing to convection and turbulent diffusion, whereas the latter becomes the similar shape to that of phase (a) or (e).

4.6. The effect of the different factors on the mass burning rate

Finally, the validated model was used to investigate the relative importance of the different influencing factors on the mass burning rate. Case 1 is the reference condition including all the influencing factors. The effects of thermocapillary force, shear stress and pressure work term (Dp_{liq}/Dt) in Eq. (9) were neglected for Cases 2, 3, and 4, respectively. For Case 5, heat transfer from the side wall of a vessel was ignored, and zero gradient condition was applied to the boundary condition for the sensible enthalpy for the liquid phase. For Case 6, gravity in the liquid phase was set to zero to examine the buoyancy effect.

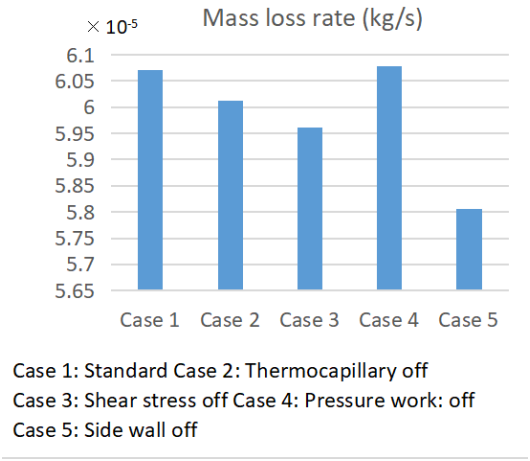

Fig. 22 The effect of different influencing factors on pool fire mass burning rates.

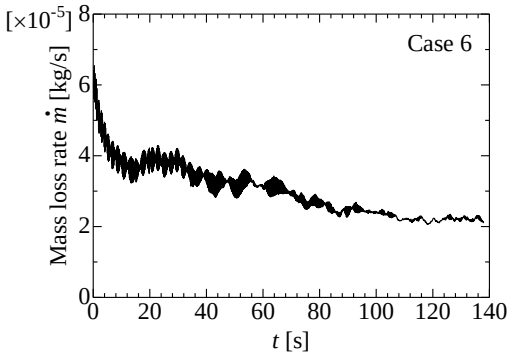

Fig. 23 The effect of gravity on the mass burning rate.

The comparison in Fig. 22 shows that the effects of thermocapillary force, shear stress, pressure work term, and heat transfer from the side wall are all less than 4%. Since it was difficult to obtain the quasi steady solution, a transient change in $\dot{m}$ is shown in Fig. 23. The predicted mean mass burning rate between 110 to 138 s is 2.1989 × 10^{-5} kg/s, which is less than 40% the matching case with gravity in Fig. 22. Since the temperature is lower at the pool bottom, distinct buoyancy is not observed in the simulations. However, the resulting density differences promote thermal mixing, resulting in liquid fuel temperature and mass burning rate for Case 1. Conversely, under zero gravity zero condition, thermal mixing is inhibited resulting in much lower liquid fuel mass burning rate. This finding indicates the potential importance of thermal mixing and convective flow in the liquid

fuel on the pool fire mass burning rate. It highlights the importance for such influence to be further investigated for larger scale pool fires.

5. Conclusions

The in-house version of the FireFOAM was modified to include a fully coupled 3-D gas-liquid approach, incorporating the effects of thermocapillary Marangoni convection, buoyancy, shear stress and evaporation in the liquid phase. Gas-liquid phase coupled simulations were conducted for the small pool fire test of Vali et al. [3]. The predicted mass burning rate, flame height, their inter-dependence and the liquid temperature distribution were all found to be in reasonably good agreement with the experimental measurements. The non-uniform temperature distribution was found near the rim owing to the difference in the distributions of convective and radiative heat fluxes, which contributed to the formation of the pair of vortices, which were experimentally observed by Vali et al. [3] and captured in the present predictions.

Numerical tests about the effects of the different influencing factors showed that the effects of the thermocapillary force, shear stress and pressure work term, and heat transfer from the side wall on the mass burning rate were relatively small and less than 4% in the presently considered cases. Conversely, the simulation assuming zero gravity resulted in almost 60% reduction in the mass burning rate. This finding indicates the potential importance of thermal mixing and convective flow within the liquid fuel on the pool fire mass burning rate. It highlights the importance for such influence to be further investigated for larger scale pool fires.

The validated model here holds potential to be applied to investigate the liquid phase transport phenomena on the mass burning rates and dynamics of pool fires of different sizes. It paves the foundation for further investigations into the liquid phase transport phenomena on the pool fire mass, burning rates, and flame evolution in transient fires of different sizes.

Acknowledgments

FireFOAM 2.2.x was built and distributed by FM Global, and the authors acknowledge technical and help supports from them. The in-house version of FireFOAM used in this study firstly developed in the project funded by the National key research and development programme special for inter-governmental cooperation (No. 2016YFE0113400) and the European Commission FP7-PEOPLE-2012-IIF (Grant number 328784).

References

[1] E.J. Weckman, A.B. Strong, Experimental investigation of the turbulence structure of medium scale methanol pool fire, Combust. Flame 105 (1996) 245–266.

[2] A. Vali, D.S. Nobes, L.W. Kostiuk, Effects of altering the liquid phase boundary conditions of methanol pool fires, Exp. Therm. Fluid Sci. 44 (2013) 786–791.

[3] A Vali, D.S. Nobes, L.W. Kostiuk, Transport phenomena within the liquid phase of a laboratory-scale circular methanol pool fire, Combust. Flame 161 (2014) 1076–1084.

[4] H. Sun, C.J. Wang, H. Liu, M. Li, A. Zhang, W. Zhao, C. Gao, Experimental study of combustion characteristics of circular ring thin-layer pool fire, Energ. Fuel 31 (2017) 10082–10092.

[5] J.X. Wen, K. Kang, T. Donchev, J.M. Karwatzki, Validation of FDS for the prediction of medium-scale pool fires, Fire Safety J. 42 (2007) 127–138.

[6] Fire Dynamics Simulator (FDS) and Smokeview (SMV), https://pages.nist.gov/fds-smv/ (accessed on 25/May/2019).

[7] Y. Wang, P. Chatterjee, J.L. de Ris, Large eddy simulation of fire plumes, Proc. Combust. Inst. 33 (2011) 2473–2480.

[8] FireFOAM 2.2.x, Source code, https://github.com/fireFoam-dev/fireFoam-2.2.x (accessed on 25/May/2019).

[9] OpenFOAM, Source code and documentations, http://www.openfoam.com/ (accessed on 25/May/2019).

[10] B.J. McCaffrey, Purely buoyant diffusion flames: some experimental results; NBSIR 79-1910, Centre for fire research, National engineering laboratory, National bureau of standards, Washington, D.C. 20234, Oct. 1979.

[11] G. Maragkos, T. Beji, B. Merci, Advances in modelling in CFD simulations of turbulent gaseous pool fires, Combust. Flame 181 (2017) 22–38.

[12] Z. Chen, J.X. Wen, B. Xu, S. Dembele, Large eddy simulation of a medium-scale methanol pool fire using the extended eddy dissipation concept, Int. J. Heat Mass Trans. 70 (2014) 389–408.

[13] B.F. Magnussen, On the structure of turbulence and a generalized eddy dissipation concept for chemical reaction in turbulent flow, 19th AIAA Aerospace Meeting, AIAA, St. Louis, USA, (1981) 1–6.

[14] K. Prasad, C. Li, K. Kailasanath, C. Ndubizu, R. Ananth, P.A. Tatem, Numerical modelling of methanol liquid pool fires, Combust. Theor. Model. 3 (1999) 743–768.

[15] V. Novozhilov, H. Koseki, CFD prediction of pool fire burning rates and flame feedback, Combust. Sci. and Technol. 176 (2004) 1283–1307.

[16] T. Sikanen, S. Hostikka, Modeling and simulation of liquid pool fires with in-depth radiation absorption and heat transfer, Fire Safety J. 80 (2016) 95–109.

[17] A. Vali, D.S. Nobes, L.W. Kostiuk, Quantifying the conduction pathways in a laboratory-scale methanol pool fire, Combust. Sci. Technol 187 (2015) 765–779.

[18] C.J. Wang, J.X. Wen, Z.B. Chen, Simulation of large-scale LNG pool fires using FireFOAM, Combust. Sci. Technol. 86 (2014) 1632–1649.

[19] K. Fukumoto, C.J. Wang, J.X. Wen, Large eddy simulation of upward flame spread on PMMA walls with a fully coupled fluid-solid approach, Combust. Flame 190 (2018) 365–387.

[20] M. Germano, U. Piomelli, P. Moin, W.H. Cabot, A dynamic subgrid-scale eddy viscosity model. Phys. Fluids A Fluid 3 (1991) 1760–1765.

[21] D.K. Lilly, A proposed modification of the Germano subgrid: scale closure method. Phys Fluids A Fluid 4 (1992) 633–633.

[22] K. Fukumoto, C.J. Wang, J.X. Wen, Large eddy simulation of a syngas jet flame: effect of preferential diffusion and detailed reaction mechanism. Energ. Fuel (2019) doi: 10.1021/acs.energyfuels.9b00130

[23] Nakakuki A. Heat transfer mechanisms in liquid pool fires. Fire Safety J. 1994;23:339–363.

[24] T.F. Smith, Z.F. Shen, J.N. Frledman, Evaluation of coefficients for the weighted sum of gray gases model, J. Heat Transfer 104 (1982) 602–608.

[25] I. Sikic, S. Dembele, J. Wen, J., Non-grey radiative heat transfer modelling in LES-CFD simulated methanol pool fires, J. Quant. Spectrosc. Ra., 234 (2019) 78–89.

[26] W. Yang W, B. Wlodzimierz, Numerical study of fuel temperature influence on single gas jet combustion in highly preheated and oxygen deficient air, Energy 30, (2005) 385–398.

[27] S.M. Ali, V. Raghavan, K. Velusamy, S. Tiwari, A numerical study of concurrent flame propagation over methanol pool surface, J. Heat Transfer 134 (2012) 1–9.

[28] J. Warnatz, U. Maas, R.W. Dibble, Combustion 4th ed. Berlin:Springer, 2006.

[29] T. Beji, B. Merci, Development of a numerical model for liquid pool evaporation, Fire Safety J. 102 (2018) 48–58.

[30] J. Chen, X. Zhang, Y. Zhao, Y. Bi, C. Li. S. Lu, Oxygen concentration effects on the burning behavior of small scale pool, Fuel 247 (2019) 378–385.

[31] B.E Poling, J.M. Prausnitz, J.P. O'Connel, The properties of gases and liquids. 5th ed., U.S. McGraw-Hill, 2001.

[32] M.D. Smooke, Reduced kinetic mechanisms and asymptotic approximations for methane-air flames, Lecture note in physics, Berlin: Springer-Verlag, 1991.

[33] A. Burcat, Thermochemical species in polynomial form, https://burcat.technion.ac.il/dir/; (accessed on 25/May/2019)

[34] Ansys.Inc. Ansys FLUENT User's Guide Release 13 2010.

[35] M. Chaos M.M. Khan, N. Krishnamoorthy, J.L de Ris, S.B. Dorofeev. Evaluation of optimization schemes and determination of solid fuel properties for CFD fire models using bench-scale pyrolysis tests. Proc. Combust. Inst. 33 (2011) 2599–2606.

[36] K. Meredith, Y. Xin, J.D. Vries, A Numerical model for simulation of thin-film water transport over solid fuel surfaces, Fire Safety Science Proceedings 10th international symposium (2011) 415–428.

[37] S.R. Turns, An introduction to combustion 2nd ed. Singapore:McGraw-Hill Education (2006).

[38] Thermal-FluidsPedia, http://www.thermalfluidscentral.org/ (accessed on 23/May/2019)

[39] E.N. Fuller, P.D. Schettler, J.C. Giddings, New method for prediction of binary gas-phase diffusion coefficients, Ind. Eng. Chem. 58 (1966) (5)

[40] A.V. Singh, M.J. Gollner, A methodology for estimation of local heat fluxes in steady laminar boundary layer diffusion flames, Combust. Flame 162 (2015) 2214–2230.

[41] H. Hayasaka, Radiative characteristics and flame structure of small-pool flames, Fire Technol. 32 (1996) 308–322.

[42] A. Vali, D.S. Nobes, L.W. Kostiuk, Characterization of flow field within the liquid phase of a small pool fire using particle image velocimetry technique, Exp Therm. Fluid Sci. 75 (2016) 228–234.

[43] N. Ren, Y. Wang, S. Vilfayeau, A. Trouvé, Large eddy simulation of vertical turbulent wall fires, Combust. Flame 169 (2016) 194–208.

[44] A. Vali, D.S. Nobes, L.W. Kostiuk, Fluid motion and energy transfer within burning liquid fuel pools of various thicknesses, Combust. Flame 162 (2015) 1477–1488.